

Journal Pre-proof

Montmorillonite-iron crosslinked alginate beads for aqueous phosphate removal

Tonoy K. Das, Quentin Scott, Achintya N. Bezbaruah



PII: S0045-6535(21)01308-4

DOI: <https://doi.org/10.1016/j.chemosphere.2021.130837>

Reference: CHEM 130837

To appear in: *ECSN*

Received Date: 13 March 2021

Revised Date: 4 May 2021

Accepted Date: 5 May 2021

Please cite this article as: Das, T.K., Scott, Q., Bezbaruah, A.N., Montmorillonite-iron crosslinked alginate beads for aqueous phosphate removal, *Chemosphere*, <https://doi.org/10.1016/j.chemosphere.2021.130837>.

This is a PDF file of an article that has undergone enhancements after acceptance, such as the addition of a cover page and metadata, and formatting for readability, but it is not yet the definitive version of record. This version will undergo additional copyediting, typesetting and review before it is published in its final form, but we are providing this version to give early visibility of the article. Please note that, during the production process, errors may be discovered which could affect the content, and all legal disclaimers that apply to the journal pertain.

© 2021 Elsevier Ltd. All rights reserved.

CRedit authorship contribution statement

Tonoy K. Das: Conceptualization, Methodology, Data curation, Formal analysis, Visualization, Writing - original draft, Investigation. **Quentin Scott:** Data curation, Visualization, Formal analysis. **Achintya N. Bezbaruah:** Supervision, Resources, Validation, Writing - review & editing, Project administration, Funding acquisition.

Journal Pre-proof

Montmorillonite-iron crosslinked alginate beads for aqueous phosphate removal

Tonoy K. Das, Quentin Scott, Achintya N. Bezbaruah*

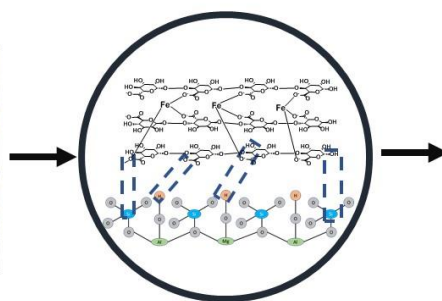
Nanoenvirology Research Group, Department of Civil and Environmental Engineering
North Dakota State University, Fargo, ND 58105, USA

*Corresponding Authors: Bezbaruah
E-mail: a.bezbaruah@ndsu.edu
Phone: (701) 231-7461

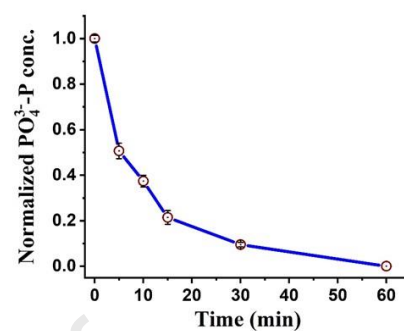
Graphical Abstract



MtIA Beads



Bead Configuration



Phosphate Removal

Journal Pre-proof

ABSTRACT

1 Phosphate runoff from agriculture fields leads to eutrophication of the water bodies with
2 devastating effects on the aquatic ecosystem. In this study, naturally occurring montmorillonite
3 clay-incorporated iron crosslinked alginate biopolymer (MtIA) beads were synthesized and
4 evaluated for aqueous phosphate removal. Batch experiment data showed an efficient phosphate
5 removal (> 99%) by the MtIA beads from solutions with different initial phosphate
6 concentrations (1 and 5 mg PO_4^{3-} -P/L, and 100 μg PO_4^{3-} -P/L). The kinetic data fitted well into
7 the pseudo-second-order kinetic model indicating chemisorption played an important role in
8 phosphate removal. Based on analyses of results from the Elovich and intra-particulate diffusion
9 models, phosphate removal by the MtIA beads was found to be chemisorption where both film
10 diffusion and intra-particulate diffusion participated. The isotherm studies indicate that MtIA
11 surfaces were heterogeneous, and the adsorption capacity of the beads calculated from Langmuir
12 model was 48.7 mg PO_4^{3-} -P/g of dry beads which is ~2.3 times higher than values reported for
13 other clay-metal-alginate beads. Electron microscopy (SEM-EDS) data from the beads showed a
14 rough-textured surface which helped the beads achieve better contact with the phosphate ions.
15 Fourier-transform infrared spectroscopy (FTIR) indicated that both iron and montmorillonite
16 clay participated in crosslinking with the alginate chain. The MtIA beads worked effectively
17 (>98% phosphate removal) over a wide pH range of 2-10 making it a robust adsorbent. The
18 beads can potentially be used for phosphate recovery from eutrophic lakes, agricultural run-off,
19 and municipal wastewater.

20 Keywords

21 Montmorillonite clay; Alginate; Iron crosslink; Phosphate; Eutrophic lakes

22 1. Introduction

23 Phosphorus (P) is one of the major growth-limiting macronutrients for plants, specifically for
24 crops. The global consumption of phosphatic fertilizer is increasing due to high-input modern
25 agricultural practices. In the last two decades, phosphatic fertilizer use increased from ~32.3
26 million tons (2000) to 45.1 million tons (2017) (FAO, 2020), and it is expected to increase
27 further as we try to meet the food demand for the rapidly growing global population. The
28 phosphorus use efficiency in our agricultural system is very low (15-20%) (Patle et al., 2019).
29 While most of the applied phosphorus gets immobilized onto the topsoil layer, and become non-
30 bioavailable to plants, and a major part ends up in different waterbodies through surface and
31 subsurface runoff as well as because of soil erosion (Kleinman et al., 2015). The excess
32 phosphorus in waterbodies causes eutrophication that triggers aquatic plant bloom and the
33 associated depletion of dissolved oxygen, and that severely affects the water quality, disrupting
34 the aquatic ecosystem (Glibert, 2020; Meinikmann et al., 2015).

35 In the United States, many waterbodies are impacted by high phosphorus concentration (with
36 $>30 \mu\text{g PO}_4^{3-}\text{-P/L}$ being eutrophic), and they include lakes ($>42\%$ of all lakes in the US) and
37 rivers/streams ($>66\%$) (USEPA, 2009). Besides adversely affecting environmental quality and
38 aquatic ecosystem, eutrophication also affects the economy by increasing the treatment needs for
39 drinking water (Duan et al., 2017), impacting fishery activities (Ruuhiarvi et al., 2010), and
40 reducing the recreational value of the waterbodies (Dodds et al., 2009). Phosphorous in
41 waterbodies are mostly orthophosphates present in very low concentrations (Boyd, 2019) yet
42 causes eutrophication ($>30 \mu\text{g PO}_4^{3-}\text{-P/L}$). There is a need to develop technologies for the
43 effective removal of aqueous phosphate specifically when present in low concentrations.

44 Phosphorus is also a non-renewable mined resource. The supply of good quality mineable rock
45 phosphate (mineral P) is predicted to last for only 60-240 years if the current consumption rate
46 continues, and it is predicted that phosphate supply will potentially fall short of demand by the
47 year 2033 (Ober, 2016). So, there is an urgent need to find alternate sources of phosphorus.
48 Phosphorus in the impaired (eutrophic) waterbodies can be one of the future sources of
49 phosphorus, and its use in agriculture would enhance sustainability by creating a cyclic process.

50 There are numerous technologies available for aqueous phosphate removals which include
51 biological methods, electrocoagulation, ion-exchange, membrane processes, and adsorption.
52 However, removal of phosphate from eutrophic lakes is very challenging given, among other
53 things, the ultra-low concentration of phosphate ($\leq 100 \mu\text{g PO}_4^{3-}\text{-P/L}$). Typical phosphate
54 concentrations reported in eutrophic lakes range from 30 to 100 $\mu\text{g PO}_4^{3-}\text{-P/L}$ (Robertson et al.,
55 2003; Wetzel, 2001). Phosphorus enters the surface waterbodies as either dissolved phosphate or
56 phosphorus loaded onto sediments and organics (Carpenter, 2005). Phosphorus strongly binds
57 with the sediments if Fe_2O_3 , CaO, and organic matters are present in sediments (Randall et al.,
58 2019), but phosphorus trapped in the legacy sediments is released to the bulk water via physico-
59 chemical and biological processes (Li et al., 2019). Reduction of internal P-loading from
60 sediments has been tried by sediment dredging (Jing et al., 2015) but that is very expensive. The
61 disposal and/or storage of dredged sediments, potential release of other toxic substances, increase
62 in phytoplankton productivity, and temporary reduction in benthic fish food (organisms) are
63 other major issues associated with dredging (Bormans et al., 2016). The addition of chemical
64 flocculants (Al-, Fe-, or Ca-based chemicals) has been proposed (Lin et al., 2015) but that
65 involves the introduction of foreign chemicals to the waterbodies and leads to the deposition of
66 P-rich sediments. In-situ sediment capping has also been proposed as a potential option for

67 remediating eutrophic waters (Wang and Jiang, 2016), but this is cost-prohibitive. Biological
68 processes like enhanced biological phosphorus removal are well established but very much
69 limited to the treatment of municipal wastewater which has high phosphate concentration (5-10
70 mg P/L) (Yang et al., 2017), and it is not feasible for use in eutrophic lakes with very low
71 aqueous phosphate (Ritt et al., 2019). Membrane processes like ultra-filtration and nanofiltration
72 can effectively remove phosphate from aqueous phase. Ion-exchange technology can also be
73 very effective. However, they are suitable for relatively small volume of water and not usable for
74 large surface waterbodies (Ritt et al., 2019). The complexity involved in the management of the
75 phosphorus cycle in eutrophic waterbodies like lakes make it very difficult to get rid phosphorus
76 totally, but we can strategize to recover the phosphate for use in agriculture (Ritt et al., 2019).

77 Adsorption is considered by many as one of the best options for phosphate removal from waters
78 (Bacelo et al., 2020; Ramasahayam et al., 2014). Adsorption technology has potential for large-
79 scale application due to its ease of implementation and economic feasibility (Kumar et al.,
80 2019a). An ideal adsorbent should be cost-effective, environmentally benign, selective for
81 phosphate with high adsorption capacity, and have quick reaction kinetics. The phosphate
82 adsorbed onto such an adsorbent should be reusable for other purposes like agriculture.

83 Clay minerals have a natural affinity for phosphate (Gérard 2016). Among the clay minerals,
84 naturally occurring montmorillonite has a relatively high specific surface area (BET specific
85 surface area of $\sim 33 \text{ m}^2/\text{g}$) and surface charge (cation exchange capacity of $\sim 85 \text{ meq}/100 \text{ g}$ of
86 clay) (Le Forestier et al., 2010). The montmorillonite clay is a 2:1 type aluminosilicate mineral
87 where one alumina octahedral sheet is sandwiched between two silica tetrahedral sheets and
88 fused together to form a one-unit cell structure (Fig. S1). The surface of the montmorillonite is

89 highly negatively charged which comes from the isomorphous substitution of lower valance
90 cations in the tetrahedral (Si^{4+} substituted by Al^{3+}) and the octahedral (Al^{3+} substituted by Mg^{2+}).

91 In this study, we used a montmorillonite clay mineral in iron crosslinked alginate biopolymer
92 beads to remove aqueous phosphate. Further, iron used for alginate crosslinking was expected to
93 crosslink with montmorillonite given its negatively charged surfaces. We used Fe^{3+} as the cross-
94 linker instead of conventional Ca^{2+} (in Ca-alginate beads) as iron and iron oxides have been
95 used as efficient phosphate adsorbents (Almeelbi and Bezbaruah, 2012; Hossain et al., 2018; Liu
96 et al., 2018). Phosphate sorption by MtIA beads was evaluated based on the data from adsorption
97 and batch kinetics studies. The role of the clay mineral in phosphate removal was investigated
98 and possible mechanisms have been proposed.

99 2. Experimental Section

100 2.1. *Chemicals and reagents*: Iron (III) chloride tetrahydrate ($\text{FeCl}_3 \cdot 4\text{H}_2\text{O}$, reagent grade, Alfa
101 Aesar, USA), monopotassium phosphate (KH_2PO_4 , 99% pure, EMD Chemicals, Germany),
102 sodium alginate ($\text{C}_6\text{H}_7\text{NaO}_6$)_n, production-grade, Spectrum Chemical, USA), sodium hydroxide
103 (NaOH , ACS Grade, BDH, USA), and Na-rich montmorillonite (SWy-2 clay, The Clay Minerals
104 Society, USA) were used as received unless otherwise specified. Laboratory produced deionized
105 (DI, 17.8 M Ω -cm) water was used in this study.

106 2.2. *Synthesis of montmorillonite clay iron crosslink beads (MtIA)*: Sodium alginate (2 g) was
107 dissolved in 50 mL of deionized (DI) water by continuous stirring and heating (~40 °C) for 1 h
108 and then the solution was continuously stirred overnight at room temperature (22±2 °C) to form
109 an alginate gel. Separately, 5 g of montmorillonite clay (Mt) was suspended in 50 mL of DI

110 water and stirred continuously until it formed a smooth slurry. The smooth clay slurry was then
111 mixed with the alginate gel and stirred continuously (at room temperature) to make a
112 homogeneous Mt-alginate solution (2% alginate and 5% clay). The Mt-alginate solution was
113 released dropwise into a ferric chloride solution (2% w/v) at room temperature using a
114 micropipette tip fitted to a silicone tube (L/S 16, Masterflex Precision Pump Tubing) connected
115 to a peristaltic pump (Masterflex, Cole-Palmer, USA) (Fig. 1a). Mt-iron crosslinked alginate
116 beads (MtIA) were formed as soon as the Mt-alginate solution came in contact with the iron
117 solution. The freshly formed beads were kept submerged in 2% FeCl_3 solution overnight (24 h)
118 in a 500 mL beaker for the beads to harden (Bezbaruah et al., 2009; Hossain et al., 2018). The
119 hardened beads were washed with a copious amount of DI water to remove the excess FeCl_3 and
120 the washed beads were stored in DI water for later use. For phosphate removal studies, the beads
121 were taken out of the water and the excess water was blotted with tissue papers. The weight of
122 the beads is reported either as wet weight or as dry weight (dried at 60 °C for 12 h). For control
123 experiments, beads were produced using the same procedure but without the Mt-clay.

124 *2.3. Material characterization:* The surface morphology of the synthesized beads was examined
125 using Scanning electron microscopy (SEM, JEOL JSM-7600F, JEOL USA, Peabody, MA). The
126 elemental composition of the beads was determined with energy-dispersive spectroscopy (EDS)
127 using UltraDry silicon drift X-ray detector and NSS-212e NORAN System 7 X-ray
128 microanalysis system (ThermoFisher Scientific, Madison, WI) which was attached to the SEM.
129 The beads were observed before and after reaction with phosphate. The samples for SEM-EDS
130 analysis were prepared by drying the beads under a vacuum condition in a nitrogen environment.
131 Dried beads (some intact and some cut in half with a razor blade to reveal the internal structure)
132 were attached to aluminum mounts with carbon tapes.

133 Fourier transform infrared (FTIR) spectra of fresh (before phosphate adsorption) and spent (after
134 phosphate adsorption) MtIA beads were recorded using a Nicolet 8700 FTIR spectrometer and
135 analyzed using OMNIC software (ThermoFisher Scientific, Waltham, MA). For FTIR analyses,
136 the beads were first dried in a vacuum oven in a nitrogen environment for 24 h, the dried beads
137 were then crushed into a fine powder. The powdered sample was mixed with potassium bromide
138 (KBr) which acted as the IR transparent background. The spectra were measured in the range of
139 4000–400 cm^{-1} with a resolution of 4 cm^{-1} and each spectrum was composed of 32 scans.

140 *2.4. Phosphate batch, kinetic and isotherm studies:* For all the phosphate removal experiments 5
141 g of wet beads (0.48 ± 0.02 g dry weight) and 45 mL of phosphate solution were placed in 50 mL
142 polypropylene plastic vials (reactors) fitted with a plastic cap. The reactors were rotated in a
143 custom-made end-over-end shaker (28 rpm) at room temperature to reduce mass transfer
144 resistance. The phosphate removal performance of the MtIA beads was determined in batch
145 experiments (24 h) with an initial phosphate concentration of 10 mg PO_4^{3-} -P/L. Controls with
146 control beads (no clay) and blanks (with no beads) were run simultaneously. The kinetics of
147 phosphate removal by MtIA beads were studied with three PO_4^{3-} -P concentrations (1 and 5
148 mg/L, and 100 $\mu\text{g/L}$). The 100 $\mu\text{g/L}$ PO_4^{3-} -P was selected as that is an environmentally relevant
149 concentration representing eutrophic lakes. A set of reactors was rotated in the end-over-end
150 shaker up to 12 h. At least three reactors were taken out at specific time intervals (0, 5, 10, 15,
151 30, 60, 180, 360, and 720 min) and the bulk solution was separated from the reactors by
152 decanting it. The bulk solution from each reactor was stored separately in the refrigerator for
153 further analysis. The phosphate concentrations in the bulk solution were measured in a Hach DR
154 5000 spectrophotometer (880 nm, detection limit 10 μg PO_4^{3-} -P/L) using the ascorbic acid
155 method (Eaton et al., 2005). The phosphate removal efficiency (η) was calculated as $\eta = (C_0 -$

156 $C_e)/C_0 \times 100\%$, where C_0 and C_e are the initial and equilibrium phosphate concentrations. The
 157 bulk solution phosphate concentration data (average of three values at each time point) were used
 158 for reaction order determination. Zero- (Eq. 1), first- (Eq. 2), second- (Eq. 3), pseudo-first- (Eq.
 159 4) (Ho and McKay, 1998), and pseudo-second- (Eq. 5) (Ho and McKay, 1998) order models
 160 were used for data analysis.

$$161 \quad C_t = C_0 - kt \quad (1)$$

$$162 \quad \ln(C_t) = \ln(C_0) - kt \quad (2)$$

$$163 \quad \frac{1}{C_t} = kt + \frac{1}{C_0} \quad (3)$$

$$164 \quad \log(q_e - q_t) = \log q_e - \frac{k_1 t}{2.303} \quad (4)$$

$$165 \quad \frac{t}{q_t} = \frac{1}{k_2 q_e^2} + \frac{t}{q_e} \quad (5)$$

166 For Eqs. 1-5, C_t is the concentration at time t , C_0 is the initial concentration, q_e (mg/g) is the
 167 equilibrium adsorption capacity of the adsorbent (beads), q_t (mg/g) is adsorption capacity at time
 168 t , k_1 (1/min) is the rate constant for the pseudo-first-order reaction, and k_2 (g/mg/min) is the rate
 169 constant for the pseudo-second-order reaction. The $\log(q_e - q_t)$ vs t plot gives the value of k_1 and
 170 q_e for the pseudo-first-order reaction, and t vs t/q_t plot helps in q_e , and k_2 determination (pseudo-
 171 second-order reaction).

172 Phosphate adsorption isotherm experiment was carried out with MtIA beads in batch reactors (5
 173 g of wet \approx 0.48 g dry beads in 45 mL solution in 50 mL reactors) with initial phosphate
 174 concentration varied from 10 to 2515 mg PO_4^{3-} -P/L. The reactors were rotated in the end-over-
 175 shaker for 24 h and the bulk solution phosphate concentration was measured. The phosphate
 176 sorption capacity was calculated as $q_e = (C_0 - C_e) \times V/m$ where q_e is the mass of phosphate per

177 gram of dry MtIA bead ($\text{mg PO}_4^{3-}\text{-P/g}$ of dry bead), V is the volume of phosphate solution (L),
178 and m is dry mass of MtIA beads (g). The adsorption isotherm data were fitted onto Langmuir
179 (Eq. 6) and Freundlich (Eq. 7) isotherm models to get insight into the adsorption mechanism.

$$180 \quad q_e = \frac{q_{\max} C_e K_L}{1 + K_L C_e} \quad (6)$$

$$181 \quad q_e = k_f C_e^{1/n} \quad (7)$$

182 In Eqs. 6 and 7, q_{\max} (mg/g) is the maximum adsorption capacity, k_L (L/mg) is the Langmuir
183 constant (which represents the affinity between the solute and adsorbent), k_f is the Freundlich
184 constant, and $1/n$ is the adsorption intensity ($1 < n < 10$). The Langmuir model represents
185 monolayer adsorption whereas the Freundlich model fits well for an adsorbent with significant
186 surface heterogeneity.

187 *2.5. Quality Control:* All experiments were performed at room temperature and in triplicate, and
188 the average values are reported here along with the standard deviations. ANOVA analyses were
189 performed using OriginLab (Version 2020) to evaluate the significant differences between the
190 data sets and Tukey's pairwise comparison was used to identify the data that were significantly
191 different.

192 **3. Results and discussion**

193 *3.1. Characterization*

194 *3.1.1. Morphology and composition:* The surface morphologies of control and MtIA beads (Fig.
195 1c-d) were observed based on SEM micrographs of the beads. Alginate beads without Mt-clay
196 (control) were also examined for comparison. While the controls (beads with no Mt-clay) had a
197 smoother surface (Fig. 1c), the MtIA bead surface (Fig. 1d) appeared as a rough-textured surface

198 due to the presence of clay particles. The surface roughness might have increased the contact
199 surface area of the beads and helped in the absorption of water and the solute (Fernandes et al.,
200 2017). Na-rich montmorillonite (SWy-2) clay has a size distribution of 5-750 nm with an
201 average size of 250 nm (Michot et al., 2004)). Montmorillonite clay minerals have surface
202 hydroxyl groups that interact with phosphate ions. Further, clay mineral surfaces act as support
203 sites for iron oxide/hydroxide formation in the MtIA beads. The bead surface did not shrink
204 when they were vacuum dried and remained spherical (Fig. 1d inset) but the controls shrunk to
205 an oblong shape (Fig. 1c inset). The EDS analysis of fresh control beads (Fig. 2a) shows carbon
206 (C), oxygen (O), iron (Fe), and chloride (Cl). The presence of a high amount of iron (~48.9%)
207 indicates that the iron was successfully incorporated within the alginate polymeric network.
208 During control bead formation sodium ion (Na^+) was replaced by iron (Fe^{3+}) through ionic
209 crosslinking to the alginate network structure (Fig. 3a). This is supported by our EDS result
210 where sodium is not detected. Further, no sodium (Na) was observed in the MtIA beads (Fig.
211 2b) even though Na^+ ion was originally present in the interlayer of Mt clay connecting two-unit
212 cell (one Al octahedral sandwich between two Si tetrahedral, Fig. 3b); this might have possibly
213 happened because the Na^+ ions were displaced during the crosslinking process. In presence of
214 water, the interlayer of Mt-clay expanded, and the iron-alginate polymer units got access to the
215 interlayer, and the polymer units expelled out the Na^+ ions from the clay minerals (Fig. 3b)
216 (Fernandes et al., 2018). The presence of high Fe and no detectable Na in MtIA beads confirms
217 this. The MtIA beads showed additional elements including magnesium (Mg), silicon (Si),
218 aluminum (Al), and potassium (K), and they came from the montmorillonite Mt-clay. There was
219 a significant reduction in the weight percent of Fe in the MtIA beads (~11.7%) compared to the
220 control beads (~48.9%). This indicates that Mt-clay particles also took part in the crosslinking

221 process (Fernandes et al., 2018; Ravi and Pandey, 2019) unlike in the control beads where Fe
222 was the main crosslinking agent.

223 3.1.2. *Fourier transform infrared spectroscopy (FTIR)*: The FTIR data were collected to gain
224 insight into the molecular interactions of freshly prepared MtIA beads (Fig. 2c) and the data were
225 compared to that obtained from the control unit. The broadband identified between 3200-3600
226 cm^{-1} in both beads corresponds to $-\text{OH}$ stretching which came from the alginate polymer chains
227 (Papageorgiou et al., 2010). Characteristic bands due to asymmetric and symmetric stretching
228 vibration of the carboxyl group of an alginate molecule appeared at 1610 and 1434 cm^{-1}
229 (Papageorgiou et al., 2010; Zhang et al., 2020) for the controls and 1628 and 1435 cm^{-1} for
230 MtIA. The asymmetric stretching vibration of a carboxylate shifted to higher wavenumbers in
231 MtIA beads (1628 cm^{-1}) compared to the control beads (1610 cm^{-1}) due to the introduction of
232 Mt-clay minerals. A group of distinguishable bands appeared in MtIA beads at 1049, 798, 626
233 cm^{-1} and could be attributed to Si–O stretching in the Si-tetrahedral of Mt-clay minerals (Barreca
234 et al., 2014; Fabryanty et al., 2017), and confirmed the presence of Mt-clay in the beads. In the
235 control beads, $-\text{CH}_2$ bending appeared at 1030 cm^{-1} and overlapped with Si–O stretching at
236 1049 cm^{-1} in the MtIA beads. The band at 1049 cm^{-1} from the MtIA beads is related to Si-O-Si
237 axial deformation into and out of the plane of the tetrahedral site (Fernandes et al., 2018). The
238 Fe–O vibration bands were identified at 510 and 468 cm^{-1} in the control beads, and 525 and 468
239 cm^{-1} in the MtIA beads, and that confirmed the successful crosslinking of alginate by iron
240 (Namduri and Nasrazadani, 2008).

241 3.2. *Batch studies for phosphate removal* and effects of pH

242 The phosphate removal performances of the MtIA bead were compared (Fig. 4a) using aqueous
243 phosphate with an initial concentration (C_0) of 10 mg PO_4^{3-} -P/L. The MtIA beads recorded ~96%
244 phosphate removal. The phosphate removal by alginate beads without Mt-clay (control) was also
245 evaluated for comparison. The MtIA beads removed 4% more phosphorus (statistically
246 significant at $p = 0.05$) than the controls (~92% phosphate removal). The higher removal by
247 MtIA beads was observed potentially because of better contact between the bead and the
248 phosphate solution due to its surface roughness (both external and internal surfaces). Further,
249 phosphate was also adsorbed onto Mt clay minerals. The effects of pH on phosphate removal (C_0
250 = 5 mg PO_4^{3-} -P/L) by the MtIA beads were monitored for a wide pH range (pH 2-10) in a DI
251 water system adjusting the initial solution pH using 0.1 M NaOH or HCL (Fig. S2a). The
252 phosphate removal remained at ~98-99% for all pH values. The point-of-zero-charge (PZC) for
253 the MtIA beads was found to be 3.14 (Fig S2 b) indicating that the surface of the beads is
254 positively charged when solution pH is below PZC and negatively charged at $\text{pH} > 3.14$ (above
255 PZC). At a pH lower than the PZC, the negatively charged phosphate ions electrostatically get
256 attached to the bead surface. With increasing pH ($\text{pH} > 3.14$), the negatively charged bead surface
257 repulses phosphate ions and that should lead to a reduction in phosphate removal. However, pH
258 was found to have minimal effect on phosphate removal by the beads (Fig S2a) indicating that
259 the removal process is not exclusively controlled by electrostatic interaction but surface
260 complexation may be involved. The versatility of the MtIA beads over a wide pH range makes
261 the beads very robust and it will work effectively in eutrophic lakes where the typical pH is 7.5-
262 8.5 (Ritt et al., 2019).

263 3.3. Removal kinetics

264 Phosphate removal by MtIA bead was evaluated at environmentally relevant high ($C_0 = 1$ and 5
265 mg PO_4^{3-} -P/L) and low ($C_0 = 100 \mu\text{g PO}_4^{3-}$ -P/L) initial concentrations (Fig. 4b-c) over a 720 min
266 (12 h) period. While 1-5 mg/L is the typical phosphate concentration in municipal wastewater,
267 $100 \mu\text{g/L PO}_4^{3-}$ -P is representative of eutrophic lakes (PO_4^{3-} -P > $30 \mu\text{g/L}$ causes eutrophication).
268 For all phosphate concentrations, MtIA beads reached equilibrium within 30 min with the
269 phosphate concentration reduced below the instrument detection limit (~100% removal). The
270 removal kinetics followed similar patterns for all the three concentrations with rapid removal in
271 the first 10 min (~62 %) followed by a relatively slow removal till an equilibrium is reached at
272 30 min.

273 To investigate the mechanism of phosphate removal by the MtIA beads and determine the rate-
274 controlling factors, the batch study data (first 60 min) were fitted into five different models
275 (zero-, first-, second-, pseudo-first-, and pseudo-second-order models) (Fig. S3-4). The data
276 fitted the best into pseudo-second-order kinetic model for all three PO_4^{3-} -P concentrations used
277 (5 mg/L: $R^2 = 0.9714$, 1 mg/L: $R^2 = 0.9996$, and $100 \mu\text{g/L}$: $R^2 = 0.9992$) (Table 1, Fig. S4).
278 Given that the data fitted into the pseudo-second-order model, we can infer that chemisorption
279 played an important role in the phosphate removal process, and the rate of adsorption was
280 proportional to the square of the number of the unoccupied sites on the adsorbent surface and the
281 concentration of adsorbate in the solution. The reaction rate constant for the pseudo-second-order
282 model increased from 0.143 ($C_0 = 5 \text{ mg PO}_4^{3-}$ -P/L) to 14.958 mg/g/min ($C_0 = 100 \mu\text{g PO}_4^{3-}$ -P/L)
283 with decreasing solution phosphate concentration (Table 1), possibly because of the abundance
284 of adsorption sites relative phosphate ions present.

285 Based on the batch study data, it can be inferred that a greater number of adsorption site were
286 potentially available for phosphate adsorption at the beginning leading to a steep concentration

287 gradient between the bead and phosphate in the bulk solution. However, the concentration
288 gradient was decreased over time, and a slower reaction was observed. The adsorption of
289 phosphate onto MtIA bead might have depended on diffusion of phosphate from bulk solution to
290 the bead's external surface (external mass transfer) or adsorption onto external surface and
291 subsequent diffusion into the internal pore (intraparticle diffusion). Kinetic data were fitted into
292 the intraparticle diffusion model (Eq. 8, after Webber and Morris, 1963 (Weber and Morris,
293 1963)) to investigate whether diffusion played any significant role in the adsorption process.

$$294 \quad q_t = k_p t^{0.5} + C \quad (8)$$

295 In Eq. 8, q_t (mg/g) is the phosphate sorption capacity of MtIA at time t (min), k_p is the intra-
296 particle diffusion rate constant ($\text{mg/g}\cdot\text{min}^{1/2}$) and C is the constant dependent on the thickness of
297 the boundary layer. C is an indicator of the boundary layer effect (the higher the value of C , the
298 greater the boundary layer effect). When q_t vs $t^{0.5}$ is plotted, k_p can be determined from the slope
299 and C from the Y-intercept (Fig. S5). If the q_t vs $t^{0.5}$ plot is a straight line and passes through the
300 origin, then intraparticle diffusion would be the only rate-limiting factor. In this study, the q_t vs
301 $t^{0.5}$ plot (Fig S5) showed bi-linearity (i.e., two steps) indicating that intraparticle diffusion was
302 not the only rate-limiting factor, but another mechanism (possibly, surface adsorption) was also
303 involved in phosphate removal. The presence of the multi-linearity of the plot (Step 1 (S_1) and
304 Step 2 (S_2)) is indicative of the presence of boundary layer diffusion and intraparticle diffusion
305 followed by saturation step. The intra-particle diffusion rate constant (k_p) was higher in S_1 step
306 compared to S_2 step for all three-phosphate concentrations tested (Table 1) indicating that
307 adsorption initially took place on an external surface with a rapid adsorption rate. When all the
308 external adsorption sites are occupied, phosphate ions started to diffuse into the internal pores of

309 the bead. The rate constant (k_p) decreased in S_2 due to increased diffusion resistance in the
310 internal pore surface and a decrease in phosphate concentration over time (Valderrama et al.,
311 2008).

312 From the pseudo-second-order model (Eq. 5), it is confirmed that chemisorption was the
313 dominant mechanism of phosphate adsorption by MtIA, and so the Elovich model (Eq. 9) was
314 used to elucidate the chemisorption process in term of variation of chemisorption energetics with
315 the extent of surface coverage (Teng and Hsieh, 1999). This model can also indicate whether the
316 active sites are heterogeneous and therefore, exhibit different activation energies for
317 chemisorption.

$$318 \quad q_t = \frac{1}{\beta} \ln(\alpha\beta) + \frac{1}{\beta} \ln(t) \quad (9)$$

319 In Eq. 9, q_t (mg/g) is the phosphate sorption capacity at time t (min) and α is the initial sorption
320 rate (mg/g-min) and β is the desorption constant (g/mg). In the plot of q_t vs $\ln(t)$, $1/\beta$ is given by
321 the slope and $1/\beta \ln(\alpha\beta)$ is the Y-intercept. The correlation coefficients (R^2) for the Elovich
322 model (Fig. S4) fitted with the experimental data for the three phosphate concentrations varied
323 from 0.9100- 0.9926 (Table 1) indicating that the adsorption of phosphate was controlled by
324 chemisorption onto heterogenous adsorption sites in the MtIA beads.

325 3.4. Adsorption isotherms

326 The experimental adsorption data (Fig. 4d) were fitted into Langmuir, Freundlich, Temkin and
327 Sips isotherm models (Table S1) to find out the type and nature of interactions of phosphate with
328 MtIA beads, adsorption mechanisms, and the maximum phosphate adsorption capacity.
329 Freundlich ($R^2 = 0.9846$) and Langmuir ($R^2 = 0.9892$) model fitted better than other isotherm

330 models (Fig. S6). The very good fit ($R^2 > 0.98$) for both the models can be explained by the
331 surface properties of the adsorbent and the affinity of the adsorbent for phosphate. That our data
332 fitted the Freundlich model well points towards surface heterogeneity of the beads as well as the
333 exponential distribution of the active sites and differences/variation in active site energies. The
334 constant k_f is related to sorption capacity and $1/n$ is an empirical parameter related to the
335 intensity of adsorption and adsorbate site heterogeneity. For $0 < 1/n < 1$, the adsorption is
336 favorable, and when $1/n$ is > 1 , the adsorption process is unfavorable, and it is irreversible when
337 $1/n = 1$. The $1/n$ value obtained from the model is 0.4703 ($0 < 1/n < 1$) which means sorption of
338 phosphate onto MtIA bead is favorable and the surface of MTIA is heterogeneous.

339 The adsorption isotherm data also fitted into the Langmuir model ($R^2 = 0.9892$). This indicates
340 that monolayer adsorption occurred on the adsorption sites of the heterogeneous beads surface
341 which consisted of several patches of smaller homogeneous surfaces, and this observation is in
342 conformity with others (Kumar et al. 2019b). The patches of homogeneous surfaces in the bead
343 included the surfaces on the clay mineral and iron-alginate complex. The maximum phosphate
344 adsorption capacity determined from the Langmuir model for MtIA is 48.78 mg PO_4^{3-} -P/g of dry
345 beads. Compared to other clay-metal ion-alginate crosslinked beads, our MtIA bead showed
346 better adsorption capacity (Table 2). Among the reported beads, zirconium (Zr)-bentonite
347 alginate beads exhibited the best adsorption capacity of 20.83 mg/g (Xi et al., 2021), and our
348 beads had ~2.3 times higher capacity than that. The Langmuir constant k_l is 0.0079 L/mg.

349 The dimensionless parameter of the equilibrium or sorption intensity (R_L) in the Langmuir model
350 (Eq. 10) was calculated using the sorption constant K_l (0.0079 L/mg) and the initial
351 concentrations of phosphate ($C_0 = 10$ to 2515 mg PO_4^{3-} -P/L) ranged from 0.0479 to 0.9268 for
352 different initial phosphate concentrations (Table S1) and that suggests that the phosphate

353 adsorption by MtIA is favorable (adsorption is unfavorable if $R_L > 1$, linear if $R_L = 1$, favorable
354 if $0 < R_L < 1$ and irreversible if $R_L = 0$ (Weber and Chakravorti, 1974).

$$355 \quad R_L = \frac{1}{1 + C_0 K_L} \quad (10)$$

356 The experimental data did not fit the Sips and Temkin models well and were not considered for
357 further evaluation.

358 3.6. Phosphate removal mechanism

359 From the adsorption kinetics and isotherm data, it is clear that phosphate adsorption onto the
360 MtIA beads is governed by chemisorption and heterogeneity of the surface of the MtIA beads.
361 There could be three possible adsorption sites in the MtIA beads which include: (1) iron present
362 in the Fe-crosslinked in alginate, (2) entrapped montmorillonite clay mineral and (3) iron sorbed
363 onto clay minerals. The phosphate removal mechanism is governed by ligand exchange, surface
364 complexation, and electrostatic attraction. Both the clay mineral surface and amorphous iron
365 oxide formed in the alginate network contain surface hydroxyl groups ($-OH$). Anionic
366 phosphates ($H_2PO_4^-/HPO_4^{2-}$) are adsorbed onto the MtIA bead surface through ligand exchange
367 between the $-OH$ groups and phosphate ions (Xu et al., 2020). Phosphate ions also replace the
368 surface $-OH$ through ion-exchange. Further, iron ions can form iron oxide and hydroxide within
369 the MtIA beads which can adsorb phosphate through inner-sphere surface complexation (Xi et
370 al., 2021). While the SEM-EDS (Fig. 5a) data confirm the adsorption of phosphate by MtIA
371 beads, the data could not pinpoint the possible active sites that adsorbed the phosphate.

372 FTIR data were collected from the fresh and spent MtIA beads to get information on molecular
373 interaction in MtIA beads as they adsorbed phosphate (Fig. 5b). The characteristic P–O

374 asymmetric bending should have appeared in the region $\sim 1030\text{ cm}^{-1}$ (Jastrzebski et al., 2011) but
375 it is not prominent enough. Therefore, the FTIR spectrum from the fresh MtIA beads was
376 subtracted from that from the spent MTIA beads, and a peak is identified at $\sim 995\text{ cm}^{-1}$ which
377 confirms the complexation of phosphate with iron oxide (Ahmed et al., 2019; Karthikeyan et al.,
378 2019).

379 **4. Conclusions**

380 In this present work, the natural montmorillonite-incorporated iron crosslinked alginate (MtIA)
381 beads designed for phosphate removal were fabricated using an easy to adopt sol-gel process. In
382 this study, both clay mineral and iron participated in the phosphate removal process. While
383 additional studies will be needed, the use of clay mineral is expected to help in making the beads
384 sturdier. Material characterization data from FTIR and SEM-EDS have indicated that both clay
385 particles and iron took part in the crosslinking with the alginate chain. The SEM micrographs of
386 MtIA beads showed a heterogeneous rough-textured surface. The surface roughness of the MtIA
387 beads facilitated the contact between phosphate ions and the beads, and thus improved the
388 phosphate removal performance by the beads. The MtIA beads also effectively ($\sim 100\%$)
389 removed low concentration phosphate ($100\text{ }\mu\text{g/L}$, eutrophic lake) within 30 min. The reaction
390 kinetic data fitted into a pseudo-second-order model indicating that the adsorption mechanism
391 was governed by chemisorption, and that was further confirmed by fitting the data into the
392 Elovich model. The adsorption data fitted in the Freundlich isotherm model ($R^2 = 0.9846$), and
393 model-derived parameters have indicated that adsorption sites in the MtIA beads are
394 heterogeneous, and adsorption of phosphate onto the MtIA bead surface is a favorable process.
395 The maximum adsorption capacity of the bead evaluated using the Langmuir model ($R^2 =$
396 0.9892) was found to be $48.78\text{ mg PO}_4^{3-}\text{-P/g}$ of dry beads which at least ~ 2.3 higher than other

397 reported values for clay-metal-alginate beads. Phosphate removal was not affected by any
398 change in pH (2-10). The beads are expected to find possible applications in phosphate removal
399 from eutrophic lakes as well as municipal wastewater and agricultural runoff (specifically, tile
400 drainage).

401 **Declaration of competing interest**

402 The authors declare that they have no known competing financial interests or personal
403 relationships that could have appeared to influence the work reported in this paper.

404 **Acknowledgments**

405 This work was funded by National Science Foundation (NSF Grant# CBET-1707093), USGS-
406 North Dakota Water Resources Research Institute, and North Dakota State University (Grand
407 Challenges Initiative). Tonoy Das received funding through NS-ICAR-IF from the Indian
408 Council of Agriculture Research. Electron microscopy was done at the NDSU Core Laboratory
409 (NSF Grant# CMMI-0821655).

410 **Appendix A. Supplementary data**

411 The following file is available free of charge: Supplementary Materials. The supporting
412 information contains additional details on Na-montmorillonite structure, kinetic study data,
413 intraparticle diffusion model data, and isotherm data.

References

- Ahmed, A.A., Gypser, S., Leinweber, P., Freese, D., Kuhn, O., 2019. Infrared spectroscopic characterization of phosphate binding at the goethite-water interface. *Physical Chemistry Chemical Physics* 21, 4421-4434.
- Almeelbi, T., Bezbaruah, A., 2012. Aqueous phosphate removal using nanoscale zero-valent iron. *Journal of Nanoparticle Research* 14.
- Bacelo, H., Pintor, A.M.A., Santos, S.C.R., Boaventura, R.A.R., Botelho, C.M.S., 2020. Performance and prospects of different adsorbents for phosphorus uptake and recovery from water. *Chemical Engineering Journal* 381, 122566.
- Barreca, S., Orecchio, S., Pace, A., 2014. The effect of montmorillonite clay in alginate gel beads for polychlorinated biphenyl adsorption: Isothermal and kinetic studies. *Applied Clay Science* 99, 220-228.
- Bezbaruah, A.N., Krajangpan, S., Chisholm, B.J., Khan, E., Bermudez, J.J.E., 2009. Entrapment of iron nanoparticles in calcium alginate beads for groundwater remediation applications. *Journal of Hazardous Materials* 166, 1339-1343.
- Bormans, M., Marsalek, B., Jancula, D., 2016. Controlling internal phosphorus loading in lakes by physical methods to reduce cyanobacterial blooms: a review. *Aquatic Ecology* 50, 407-422.
- Boyd, C.E., 2019. Phosphorus. In: *Water quality: An Introduction*. Springer Nature.
- Carpenter, S.R., 2005. Eutrophication of aquatic ecosystems: Bistability and soil phosphorus. *Proceedings of the National Academy of Sciences of the United States of America* 102, 10002-10005.
- Dodds, W.K., Bouska, W.W., Eitzmann, J.L., Pilger, T.J., Pitts, K.L., Riley, A.J., Schloesser, J.T., Thornbrugh, D.J., 2009. Eutrophication of US Freshwaters: Analysis of Potential Economic Damages. *Environmental Science & Technology* 43, 12-19.
- Duan, H.T., Tao, M., Loisel, S.A., Zhao, W., Cao, Z.G., Ma, R.H., Tang, X.X., 2017. MODIS observations of cyanobacterial risks in a eutrophic lake: Implications for long-term safety evaluation in drinking-water source. *Water Research* 122, 455-470.
- Eaton, A., Clesceri, L.S., Rice, E.W., Greenberg, A.E., Franson, M., 2005. *APHA: standard methods for the examination of water and wastewater. Centennial Edition.*, APHA, AWWA, WEF, Washington, DC.
- Fabryanty, R., Valencia, C., Soetaredjo, F.E., Putro, J.N., Santoso, S.P., Kurniawan, A., Ju, Y.H., Ismadji, S., 2017. Removal of crystal violet dye by adsorption using bentonite - alginate composite. *Journal of Environmental Chemical Engineering* 5, 5677-5687.
- Food and Agriculture Organization (FAO) FAOSTAT: Fertilizers Archive 2020. Available at <http://www.fao.org/faostat/en/#data/RA> (Accessed March, 2021)
- Fernandes, R.D., de Moura, M.R., Glenn, G.M., Aouada, F.A., 2018. Thermal, microstructural, and spectroscopic analysis of Ca²⁺ alginate/clay nanocomposite hydrogel beads. *Journal of Molecular Liquids* 265, 327-336.
- Fernandes, R.S., de Moura, M.R., Aouada, F.A., 2017. Optimization of synthesis of intercalated nanocomposite hidrogels for future application in the medical area. *Quimica Nova* 40, 60-67.
- Gérard, F., 2016. Clay minerals, iron/aluminum oxides, and their contribution to phosphate sorption in soils—A myth revisited. *Geoderma*, 262, 213-226.

- Glibert, P.M., 2020. Harmful algae at the complex nexus of eutrophication and climate change. *Harmful Algae* 91.
- Ho, Y.S., McKay, G., 1998. Kinetic models for the sorption of dye from aqueous solution by wood. *Process Safety and Environmental Protection* 76, 183-191.
- Hossain, M. E., Ritt, C. L., Almeelbi, T. B., & Bezbaruah, A. N. 2018. Biopolymer beads for aqueous phosphate removal: possible applications in eutrophic lakes. *Journal of Environmental Enginerring* 144(5), 04018030.
- Jastrzebski, W., Sitarz, M., Rokita, M., Bulat, K., 2011. Infrared spectroscopy of different phosphates structures. *Spectrochimica Acta Part a-Molecular and Biomolecular Spectroscopy* 79, 722-727.
- Jing, L.D., Liu, X.L., Bai, S., Wu, C.X., Ao, H.Y., Liu, J.T., 2015. Effects of sediment dredging on internal phosphorus: A comparative field study focused on iron and phosphorus forms in sediments. *Ecological Engineering* 82, 267-271.
- Karthikeyan, P., Banu, H.A.T., Meenakshi, S., 2019. Synthesis and characterization of metal loaded chitosan-alginate biopolymeric hybrid beads for the efficient removal of phosphate and nitrate ions from aqueous solution. *International Journal of Biological Macromolecules* 130, 407-418.
- Kleinman, P.J.A., Sharpley, A.N., Withers, P.J.A., Bergstrom, L., Johnson, L.T., Doody, D.G., 2015. Implementing agricultural phosphorus science and management to combat eutrophication. *Ambio* 44, S297-S310.
- Kumar, P.S., Korving, L., van Loosdrecht, M.C.M., Witkamp, G.J., 2019a. Adsorption as a technology to achieve ultra-low concentrations of phosphate: Research gaps and economic analysis. *Water Research X* 4.
- Kumar, V.K., Srinivas, G., Wood, B., Ramisetty, K.A., Stewart, A.A., Howard, C.A., Brett, D. and Rodriguez-Reinoso, F., 2019b. Characterization of adsorption site energies and heterogeneous of porous materials. *Journal of Materials Chemistry A* 7,10104.
- Kumar, I.A., Viswanathan, N., 2017. Fabrication of metal ions cross-linked alginate assisted biocomposite beads for selective phosphate removal. *Journal of Environmental Chemical Engineering* 5, 1438-1446.
- Kumar, I.A., Viswanathan, N., 2020. Fabrication of zirconium(IV) cross-linked alginate/kaolin hybrid beads for nitrate and phosphate retention. *Arabian Journal of Chemistry* 13, 4111-4125.
- Le Forestier, L., Muller, F., Villieras, F., Pelletier, M., 2010. Textural and hydration properties of a synthetic montmorillonite compared with a natural Na-exchanged clay analogue. *Applied Clay Science* 48, 18-25.
- Li, X.D., Zhang, Z.Y., Xie, Q., Yang, R.J., Guan, T., Wu, D.Y., 2019. Immobilization and Release Behavior of Phosphorus on Phoslock-Inactivated Sediment under Conditions Simulating the Photic Zone in Eutrophic Shallow Lakes. *Environmental Science & Technology* 53, 12449-12457.
- Lin, J., Qiu, P.H., Yan, X.J., Xiong, X., Jing, L.D., Wu, C.X., 2015. Effectiveness and Mode of Action of Calcium Nitrate and Phoslock (R) in Phosphorus Control in Contaminated Sediment, a Microcosm Study. *Water Air and Soil Pollution* 226.
- Liu, R.T., Chi, L.N., Wang, X.Z., Sui, Y.M., Wang, Y., Arandiyan, H., 2018. Review of metal (hydr)oxide and other adsorptive materials for phosphate removal from water. *Journal of Environmental Chemical Engineering* 6, 5269-5286.
- Meinikmann, K., Hupfer, M., Lewandowski, J., 2015. Phosphorus in groundwater discharge - A potential source for lake eutrophication. *Journal of Hydrology* 524, 214-226.

- Michot, L.J., Bihannic, I., Porsch, K., Maddi, S., Baravian, C., Mougél, J. and Levitz, P., 2004. Phase diagrams of Wyoming Na-montmorillonite clay. Influence of particle anisotropy. *Langmuir*, 20(25), 10829-10837.
- Namduri, H., Nasrazadani, S., 2008. Quantitative analysis of iron oxides using Fourier transform infrared spectrophotometry. *Corrosion Science* 50, 2493-2497.
- Ober, J.A., 2016. Mineral commodity summaries 2016. US Geological Survey.
- Papageorgiou, S.K., Kouvelos, E.P., Favvas, E.P., Sapalidis, A.A., Romanos, G.E., Katsaros, F.K., 2010. Metal-carboxylate interactions in metal-alginate complexes studied with FTIR spectroscopy. *Carbohydrate Research* 345, 469-473.
- Patle, T., Khaddar, V., Tiwari, R., Para, P., 2019. Evaluation of phosphorus availability and phosphorus fixation in four different soils orders. *Journal of Pharmacognosy and Phytochemistry* 8, 2087-2090.
- Pawar, R.R., Gupta, P., Lalhmunsiana, Bajaj, H.C., Lee, S.M., 2016. Al-intercalated acid activated bentonite beads for the removal of aqueous phosphate. *Science of the Total Environment* 572, 1222-1230.
- Ramasahayam, S.K., Guzman, L., Gunawan, G., Viswanathan, T., 2014. A Comprehensive Review of Phosphorus Removal Technologies and Processes. *Journal of Macromolecular Science Part a-Pure and Applied Chemistry* 51, 538-545.
- Randall, M.C., Carling, G.T., Dastrup, D.B., Miller, T., Nelson, S.T., Rey, K.A., Hansen, N.C., Bickmore, B.R., Aanderud, Z.T., 2019. Sediment potentially controls in-lake phosphorus cycling and harmful cyanobacteria in shallow, eutrophic Utah Lake. *Plos One* 14.
- Ravi, Pandey, L.M., 2019. Enhanced adsorption capacity of designed bentonite and alginate beads for the effective removal of methylene blue. *Applied Clay Science* 169, 102-111.
- Ritt, C.L., Chisholm, B.J., Bezbaruah, A.N., 2019. Assessment of molecularly imprinted polymers as phosphate sorbents. *Chemosphere* 226, 395-404.
- Robertson, D.M., Rose, W.J., Saad, D.A., 2003. Water quality and the effects of changes in phosphorus loading to Muskellunge Lake, Vilas County, Wisconsin. US Department of the Interior, US Geological Survey.
- Ruuhijarvi, J., Rask, M., Vesala, S., Westermark, A., Olin, M., Keskitalo, J., Lehtovaara, A., 2010. Recovery of the fish community and changes in the lower trophic levels in a eutrophic lake after a winter kill of fish. *Hydrobiologia* 646, 145-158.
- Teng, H., Hsieh, C.T., 1999. Activation energy for oxygen chemisorption oil carbon at low temperatures. *Industrial & Engineering Chemistry Research* 38, 292-297.
- US Environmental Protection Agency (USEPA), 2009. Nutrient control design manual: state of technology review report. EPA/600/R-09/012 EPA/600/R-09/012.
- Valderrama, C., Gamisans, X., de las Heras, X., Farran, A., Cortina, J.L., 2008. Sorption kinetics of polycyclic aromatic hydrocarbons removal using granular activated carbon: Intraparticle diffusion coefficients. *Journal of Hazardous Materials* 157, 386-396.
- Wang, C.H., Jiang, H.L., 2016. Chemicals used for in situ immobilization to reduce the internal phosphorus loading from lake sediments for eutrophication control. *Critical Reviews in Environmental Science and Technology* 46, 947-997.
- Wang, B., Zhang, W., Li, L., Guo, W.B., Xing, J., Wang, H.Y., Hu, X.L., Lyu, W.L., Chen, R.F., Song, J.Y., Chen, L., Hong, Z.Z., 2020. Novel talc encapsulated lanthanum alginate hydrogel for efficient phosphate adsorption and fixation. *Chemosphere* 256.
- Weber, T.W., Chakravorti, R.K., 1974. Pore and solid diffusion models for fixed-bed adsorbers. *Aiche Journal* 20, 228-238.

- Weber, W.J., Morris, J.C., 1963. Kinetics of adsorption on carbon from solution. *Journal of the Sanitary Engineering Division* 89, 31-60.
- Wetzel, R.G., 2001. *Limnology: lake and river ecosystems*. Gulf Professional Publishing.
- Xi, H., Li, Q.Q., Yang, Y., Zhang, J.F., Guo, F., Wang, X.G., Xu, S.K., Ruan, S.P., 2021. Highly effective removal of phosphate from complex water environment with porous Zr-bentonite alginate hydrogel beads: Facile synthesis and adsorption behavior study. *Applied Clay Science* 201.
- Xu, X.Y., Wang, B., Tang, H., Jin, Z.X., Mao, Y.L., Huang, T.Y., 2020. Removal of phosphate from wastewater by modified bentonite entrapped in Ca-alginate beads. *Journal of Environmental Management* 260.
- Yang, Y., Shi, X., Ballent, W., Mayer, B.K., 2017. Biological Phosphorus Recovery: Review of Current Progress and Future Needs. *Water Environment Research* 89, 2122-2135.
- Zhang, H.Y., Shi, Y.S., Xu, X.F., Zhang, M., Ma, L., 2020. Structure Regulation of Bentonite-Alginate Nanocomposites for Controlled Release of Imidacloprid. *ACS Omega* 5, 10068-10076.

LIST OF TABLES:

Table 1. Kinetic parameters associated with phosphate adsorption by the MtIA beads.

Table 2. Phosphate adsorption performance of different clay-metal ion-alginate crosslinked beads.

LIST OF FIGURES:

Fig. 1. (a) Schematic of montmorillonite iron crosslinked alginate (MtIA) bead synthesis process. (b) Photograph of freshly produced MtIA beads; (c) SEM micrograph of a control bead; and (d) SEM micrograph of a MtIA bead with each inset showing a cross-section of the bead. The surface of the control bead was smooth, and the bead shrunk to become oblong upon drying. The MtIA bead surface showed rough texture due to the presence of the clay mineral, the bead maintained its spherical shape upon drying.

Fig. 2. SEM-EDS of (a) control bead; (b) MtIA bead. There was a significant decrease in iron content in the MtIA beads (~11.7%) compared to the control beads (~48.9%). In the MtIA beads, noticeable amounts of Si and Al were recorded which came from Mt-clay (aluminosilicate); and (c) FTIR spectra for the control and MtIA beads. The broadband of 3200-3600 cm^{-1} in both spectra came from -OH stretching of alginate polymer. The carboxylate asymmetric stretching vibration shifted in MtIA (1628 cm^{-1}) and control (1610 cm^{-1}) confirming the introduction of the clay mineral in the alginate network. Further, characteristic peak Fe-O vibration appeared in each polymer bead confirming Fe-ion crosslinking with alginate.

Fig. 3. (a) Possible crosslinking process of Fe^{3+} to the alginate network and interaction with clay mineral surface. Crosslinked alginate chain and silicate clay layer are connected at several points

through electrostatic and intermolecular hydrogen bonds which create a three-dimensional network; and (b) Possible clay polymer network configuration. The iron crosslinked alginate accesses the interlayer between two montmorillonite units and expels the interlayer Na^+ (Figures modified after Fernandes et al., 2018).

Fig. 4. (a) Phosphate removal by MtIA beads ($C_0 = 10 \text{ mg PO}_4^{3-}\text{-P/L}$, Adsorbent dose = 5 g wet beads in 45 mL solution); and (b) Phosphate removal by MtIA beads over time from solutions with two different initial $\text{PO}_4^{3-}\text{-P}$ concentrations (5 and 1 mg/L). Inset: the first 60 min zoomed in; (c) solution with initial $\text{PO}_4^{3-}\text{-P}$ concentration of 100 $\mu\text{g/L}$); and (d) Adsorption isotherm for phosphate sorption onto MtIA. The data points are connected with straight lines for ease of reading only and they do not represent trendlines. The vertical error bars represent \pm standard deviations.

Fig. 5. (a) EDS spectra of spent MtIA beads (i.e., after phosphate adsorption); (b) FTIR spectra of MtIA beads before and after phosphate adsorption. Inset: Spectra at $\sim 995 \text{ cm}^{-1}$ in the spent beads confirmed the formation of iron-phosphate compounds (The spectrum obtained from the fresh MtIA beads was subtracted from that of the spent MtIA beads).

Table 1. Kinetic parameters associated with phosphate adsorption by the MtIA beads.

Kinetics Model	Parameter	Phosphate Concentration					
		5 mg/L		1 mg/L		100 µg/L	
Pseudo-second Order	R^2	0.9714		0.9996		0.9992	
	q_e	0.610		0.106		0.010	
	k_2	0.143		1.043		14.958	
Intra-particle Diffusion	R^2	0.7815		0.9297		0.9000	
		S_1	S_2	S_1	S_2	S_1	S_2
	R_i^2	0.9653	0.712	0.9870	0.9843	0.9833	0.9737
	k_p	0.1444	0.0302	0.0172	0.0068	0.0016	0.0005
	C	-0.1718	0.2809	0.0005	0.0409	0.0008	0.0054
Elovich-Mass Transfer	R^2	0.9100		0.9926		0.9733	
	α	0.1036		0.0278		526.315	
	β	6.8634		45.8715		4.1842×10^{-3}	

Units: q_e : mg/g; K_2 : mg/g/min; k_p : mg/g min^{1/2}; C : mg/g; α : mg/g/min; β : g/mg. Notes: R^2 : Overall correlation coefficient; R_i^2 : Correlation coefficient for each step in the intra-particle diffusion model; S_1 : Step 1 and S_2 : Step 2 in the intra-particle diffusion model.

Table 2. Phosphate adsorption performance of different clay-metal ion-alginate crosslinked beads.

Alginate Bead composition	Cross-linking ion	Solution pH	Concentration range (mg/L) tested	Dose (dry bead, g/L)	Adsorption capacity (PO ₄ ³⁻ -P mg/g)	Source
Zr-Alginate Bentonite	Zr ⁴⁺	-	-	2	9.89	(Kumar and Viswanathan, 2017)
Ce-Alginate Bentonite	Ce ³⁺	-	-	2	8.52	(Kumar and Viswanathan, 2017)
La-Alginate Bentonite	La ³⁺	-	-	2	6.74	(Kumar and Viswanathan, 2017)
La-alginate-talc	La ³⁺	4	2.5-50	0.4	16.4	(Wang et al., 2020)
Zr-alginate assisted kaolin	Zr ⁴⁺	-	0-45	2	12.12	(Kumar and Viswanathan, 2020)
Zr-bentonite alginate	Zr ⁴⁺	7	1.6-65	-	20.83	(Xi et al., 2021)
Al-modified bentonite alginate	Ca ²⁺	3	1.6-13	2.6	5.14	(Xu et al., 2020)
Al-pillared activated bentonite alginate	Ca ²⁺	5	2-27	2	6.23	(Pawar et al., 2016)
MtIA beads	Fe ³⁺	6.5-7	0-2500	10.66	47.8	This study

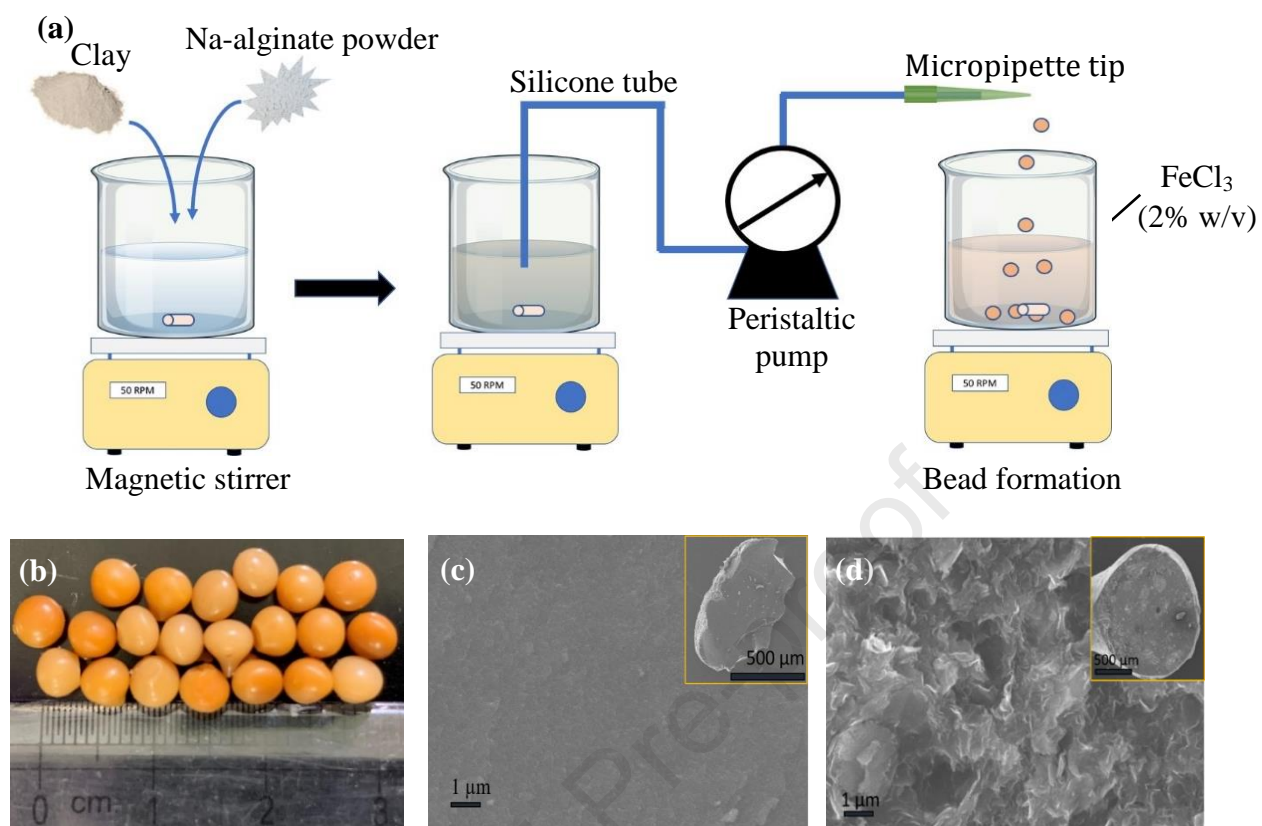


Fig. 1.

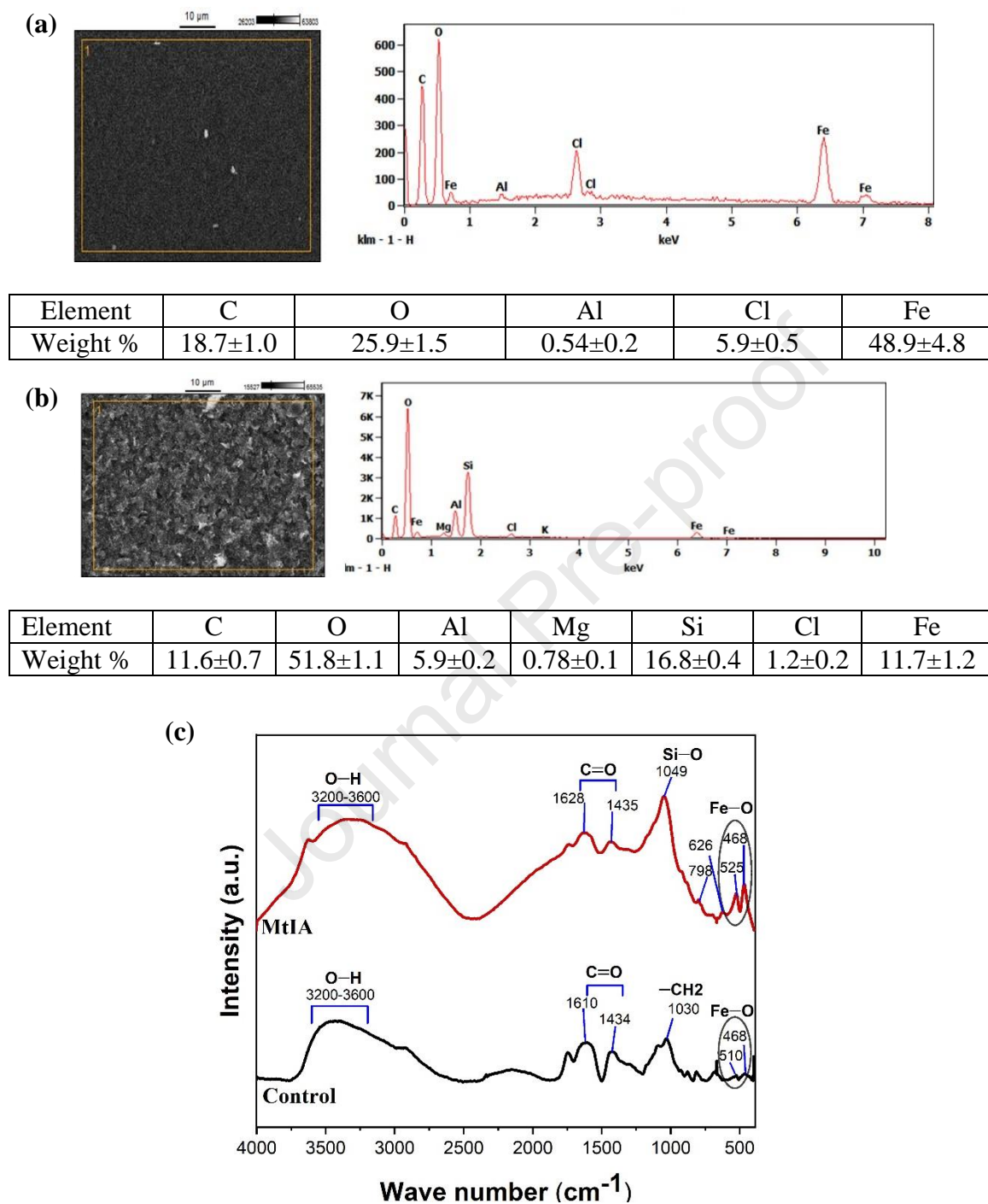


Fig. 2.

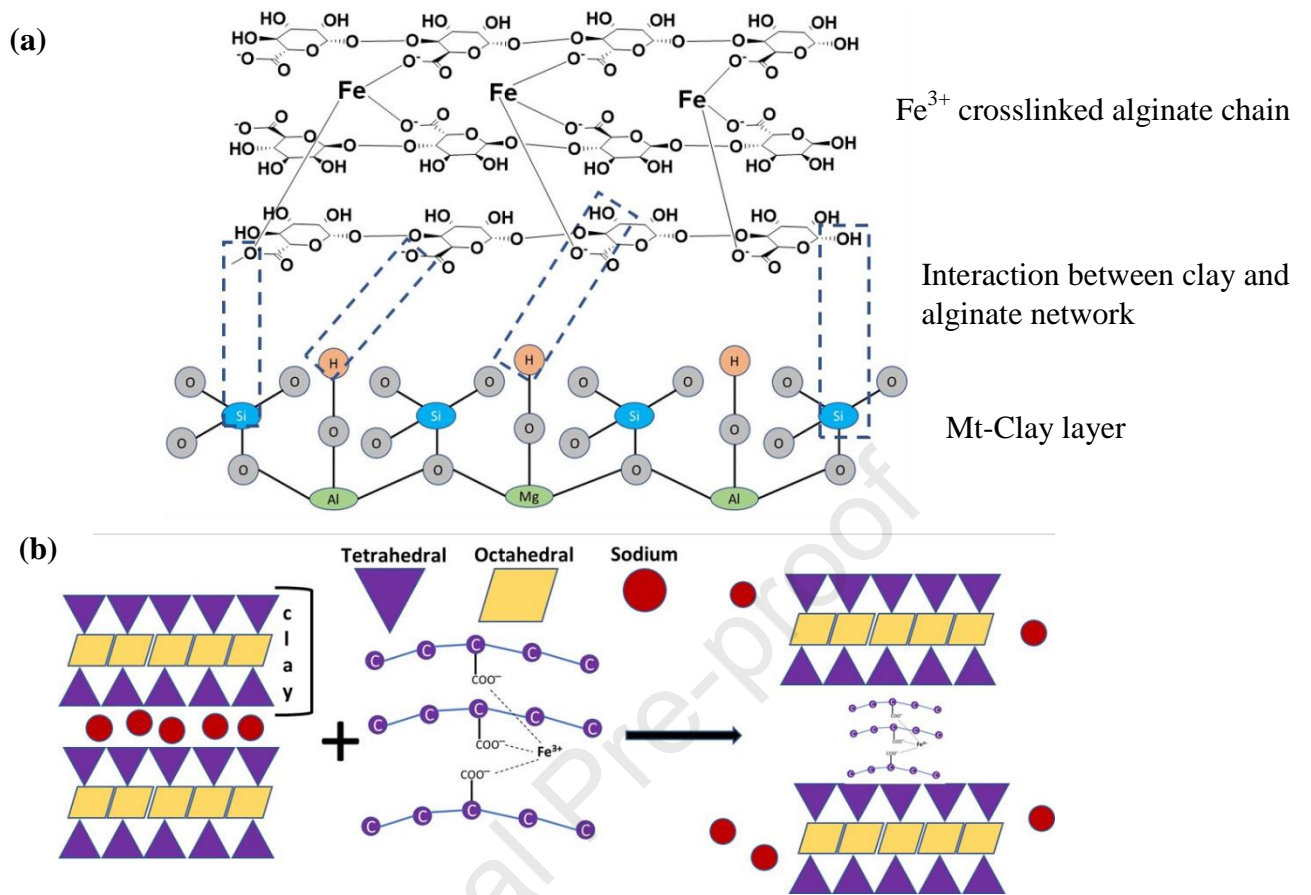


Fig. 3.

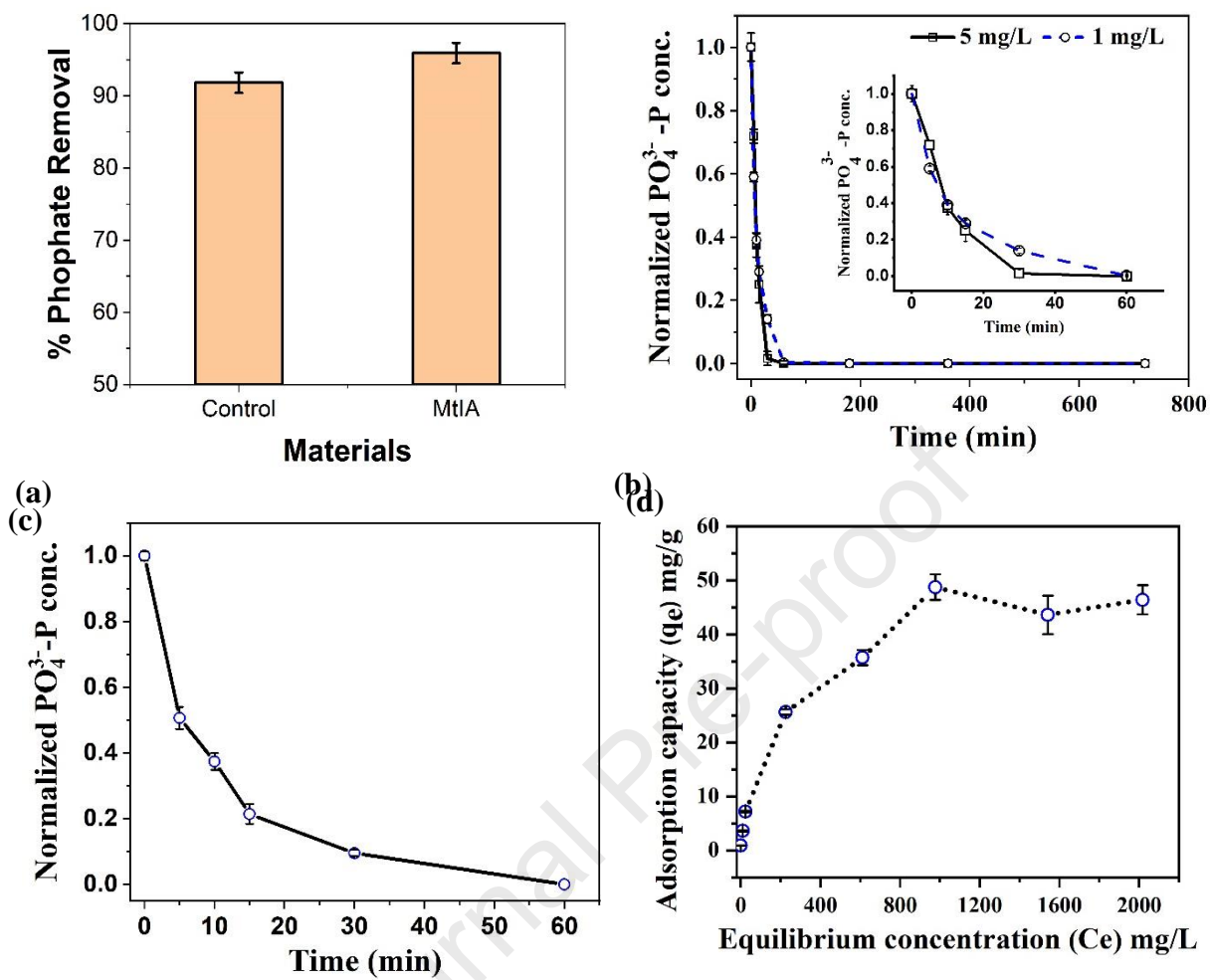
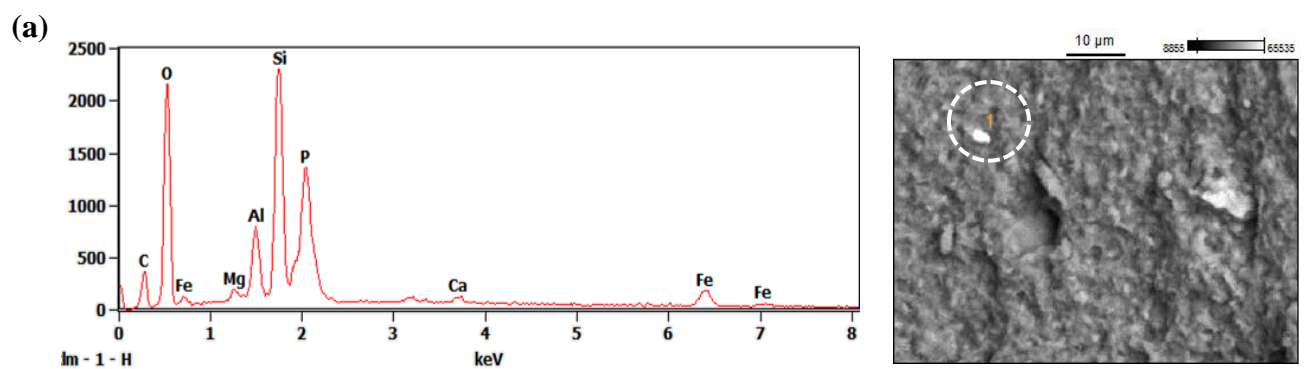


Fig. 4.



Element	C	O	Mg	Al	Si	P	Ca	Fe
Weight %	9.8 \pm 0.7	38.3 \pm 1.2	0.61 \pm 0.3	5.2 \pm 0.4	18.5 \pm 0.8	13.2 \pm 0.9	1.5 \pm 0.6	12.8 \pm 2.2

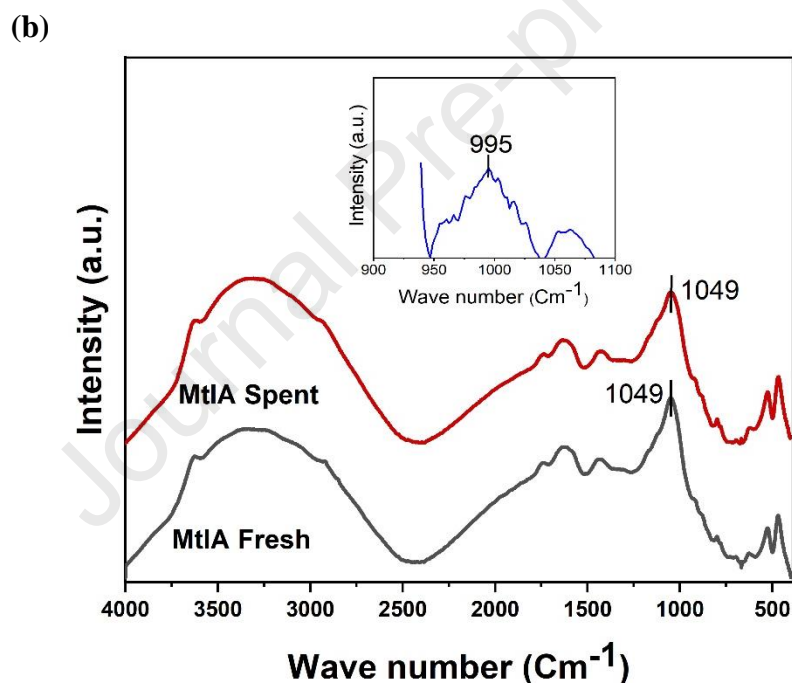


Fig. 5.

Highlights

- Facile synthesis of montmorillonite iron crosslinked alginate (MtIA) beads.
- MtIA beads had an adsorption capacity of 47.8 mg $\text{PO}_4^{3-}\text{-P/g}$ of dry weight
- The beads effectively removed phosphate (>99%) even at low concentrations (100 $\mu\text{g PO}_4^{3-}\text{-P/L}$).
- The beads showed fast kinetics and reached equilibrium in < 30 min.
- Phosphate removal was via chemisorption onto the heterogeneous adsorption sites in the beads.

Declaration of interests

The authors declare that they have no known competing financial interests or personal relationships that could have appeared to influence the work reported in this paper.

The authors declare the following financial interests/personal relationships which may be considered as potential competing interests:

Achintya Bezbaruah
Tonoy Das
Quentin Scott
March 11, 2021

Journal Pre-proof